

NHWAVE: Consistent boundary conditions and turbulence modeling



Morteza Derakhti^{a,*}, James T. Kirby^a, Fengyan Shi^a, Gangfeng Ma^b

^a Center for Applied Coastal Research, University of Delaware, Newark, DE, USA

^b Department of Civil and Environmental Engineering, Old Dominion University, Norfolk, VA, USA

ARTICLE INFO

Article history:

Received 1 June 2015

Revised 29 July 2016

Accepted 8 September 2016

Available online 12 September 2016

Keywords:

Non-hydrostatic model

Dynamic boundary conditions

Wave breaking

ABSTRACT

Large-scale σ -coordinate ocean circulation models neglect the horizontal variation of σ in the calculation of stress terms and boundary conditions. Following this practice, the effects of surface and bottom slopes in the dynamic surface and bottom boundary conditions have been usually neglected in the available non-hydrostatic wave-resolving models using a terrain-following grid. In this paper, we derive consistent surface and bottom boundary conditions for the normal and tangential stress fields as well as a Neumann-type boundary condition for scalar fluxes. Further, we examine the role of surface slopes in the predicted near-surface velocity and turbulence fields in surface gravity waves. By comparing the predicted velocity field in a deep-water standing wave in a closed basin, we show that the consistent boundary conditions do not generate unphysical vorticity at the free surface, in contrast to commonly used, simplified stress boundary conditions developed by ignoring all contributions except vertical shear in the transformation of stress terms. In addition, it is shown that the consistent boundary conditions significantly improve predicted wave shape, velocity and turbulence fields in regular surf zone breaking waves, compared with the simplified case. A more extensive model-data comparison of various breaking wave properties in different types of surface breaking waves is presented in companion papers (Derakhti et al., 2016a,b).

© 2016 Elsevier Ltd. All rights reserved.

1. Introduction

Surface wave breaking plays an important role in numerous environmental and technical processes such as air-sea interaction, acoustic underwater communications, optical properties of the water column, nearshore mixing and coastal morphodynamics. Wave breaking is a highly dissipative process, limiting the maximum height of surface waves. It is also a source of turbulence, enhancing transport and mixing in the ocean surface layer (Banner and Peregrine, 1993; Melville, 1996; Duncan, 2001; Perlin et al., 2013).

Although large-eddy simulations (LES) combined with the volume-of-fluid (VOF) method for free-surface tracking (Watanabe et al., 2005; Derakhti and Kirby, 2014; 2016) can resolve turbulence and mean flow dynamics in breaking waves quite well, they are computationally expensive even for laboratory-scale events. A lower-resolution framework is needed to study long-term, $\mathcal{O}(\text{days})$, and large-scale, $\mathcal{O}(100 \text{ m} \sim 10 \text{ km})$, wave-breaking-driven circulation as well as transport of sediment, bubbles, and other suspended materials. Computationally efficient Boussinesq-type models (e.g., Wei et al., 1995; Shi et al., 2012) can often yield accept-

able predictions of surface elevations and depth-averaged currents in the nearshore region. Such single layer models, however, cannot provide the vertical structure of mean flow or information on instantaneous motion over rapidly-varying bathymetry or current fields, and thus recourse must be made to models which either provide estimates of vertical structures through closure hypotheses (Kim et al., 2009) or which utilize a three-dimensional (3D) framework from the outset.

During the past two decades, several multi-layered wave-resolving non-hydrostatic models based on Reynolds-averaged Navier–Stokes (RANS) equations, such as Stansby and Zhou (1998), Lin and Li (2002), Bradford (2011) and Ma et al. (2012), have been developed for coastal applications using surface- and terrain-following curvilinear (x, y, σ) coordinates, hereafter referred as the σ -coordinate system. In comparison with VOF-based models, a direct simplification of this new framework is achieved by assuming the free surface to be a single-valued function of horizontal location. By using a σ -coordinate system, the free surface is always located at an upper computational boundary, determined by applying free-surface boundary conditions. Using a Keller-box scheme, a pressure boundary condition at the free surface can thus be accurately prescribed, and dispersion characteristics of short waves are typically predicted accurately using a few vertical σ -levels.

* Corresponding author.

E-mail address: derakhti@udel.edu (M. Derakhti).

However, the effects of surface and bottom slopes in the dynamic boundary conditions at the top and bottom interfaces, e.g., the continuity of the tangential surface stress, have been ignored in most of the previous non-hydrostatic studies using a terrain-following grid, following the previous practice in large-scale ocean circulation models. In the absence of surface wind stress, the simplified tangential stress boundary condition at the free surface developed by ignoring all contributions except vertical shear in the transformation of tangential stress, reads as (Lin and Li (2002, equation 41), Bradford (2011, equation 22) and Ma et al. (2012, equation 36))

$$\frac{\partial u_i}{\partial z} = \frac{1}{D} \frac{\partial u_i}{\partial \sigma} = 0, \quad (1)$$

where $i = 1, 2$ and u_i is the horizontal velocity component in the i direction. In intermediate and deep water, we have

$$\omega_y = \frac{\partial u}{\partial z} - \frac{\partial w}{\partial x} = \frac{u_0}{L_0} \left(\frac{\partial u'}{\partial z'} - \frac{\partial w'}{\partial x'} \right) \sim \frac{\varepsilon c_0}{L_0} \sim \varepsilon f_0 \quad (2)$$

where ω_y is the vorticity component in the y direction, L_0 and u_0 are the length and velocity scales respectively, for both the horizontal and vertical directions. Here, c_0 and f_0 are the wave's phase speed and frequency respectively, $\varepsilon = a_0/L_0$ is the wave steepness, and a_0 is the wave amplitude. Thus, imposing (1) generates error in wave vorticity divided by wave frequency to $\mathcal{O}(\varepsilon)$, the order of the motion itself. In other words, imposing (1) at the free surface acts as an unphysical local source of vorticity of strength $\partial w/\partial x$ which in turn generates an unphysical near-surface residual circulation.

In breaking waves, the surface slopes are large, $\mathcal{O}(1)$, and $\partial u_i/\partial \sigma \neq 0$ in a bore-like region, and thus using (1) provides a poor estimation of the associated near-surface velocity gradient and turbulence production. Another simplification in some of the existing non-hydrostatic RANS models using the σ -coordinate system is the neglect of the effects of surface and bottom slopes in the horizontal diffusion terms (Stansby and Zhou, 1998).

Our goals here are (1) to derive consistent surface and bottom dynamic boundary conditions for the normal and tangential stress fields and (2) to carefully examine the role of surface slopes in the predicted near-surface velocity and turbulence fields in surface gravity waves. We compare the velocity field in a deep-water standing wave in a closed basin predicted by the new version of the non-hydrostatic model NHWAVE with that predicted by a previous version of the model (Ma et al., 2012) (hereafter referred to as the original model), showing that the consistent boundary conditions do not generate unphysical vorticity at the free surface, in contrast to commonly used, simplified stress boundary conditions developed by ignoring all contributions except vertical shear in the transformation of stress terms. In addition, it is shown that the consistent boundary conditions significantly improve the predicted wave shape and wave heights as well as velocity and turbulence fields in regular surf zone breaking waves, compared with the simplified case.

The paper is organized as follows. In Section 2, we present the governing equations, in conservative form, describing a complete form of the RANS equations in the σ -coordinate system together with various turbulence closure models. In Section 3, we derive the consistent surface and bottom dynamic boundary conditions for the velocity and dynamic pressure fields, using the appropriate dynamic boundary conditions on normal and tangential stresses at the top and bottom interfaces as well as a Neumann-type boundary condition for scalar fluxes. In Section 4, we examine the role of surface slopes in the near-surface velocity and turbulence fields in surface gravity waves. Wave-breaking-induced eddy viscosity and its effect on the wave height distribution in the surf zone are discussed in Section 5. Conclusions are given in Section 6. A more

extensive model-data comparison of various breaking wave properties in different types of surface breaking waves is presented in companion papers (Derakhti et al., 2016a,b).

2. Governing equations in conservative form

Here, the complete and conservative form of the RANS equations and the scalar transport equation in the σ -coordinate system are presented. Further, different turbulence models including the standard $k - \varepsilon$ (Rodi, 1980) and the renormalization group (RNG) approach by Yakhot et al. (1992), are presented. The surface and bottom boundary conditions will be derived in the next section. Details of the numerical method may be found in Ma et al. (2012) and Derakhti et al. (2015).

2.1. Continuity and momentum equations

Assuming a uniform density field, the RANS equations in Cartesian coordinates (x_1^*, x_2^*, x_3^*) , where $x_1^* = x^*$, $x_2^* = y^*$ and $x_3^* = z^*$ reads as

$$\frac{\partial u_j}{\partial x_j^*} = 0 \quad (3)$$

$$\frac{\partial u_i}{\partial t^*} + \frac{\partial u_i u_j}{\partial x_j^*} = \frac{1}{\rho_0} \frac{\partial \mathcal{S}_{ij}}{\partial x_j^*} + g_i \delta_{i3}, \quad (4)$$

where $(i, j) = 1, 2, 3$, u is the ensemble-averaged velocity, ρ_0 is the reference water density, $\mathbf{g} = (0, 0, -g)$ is the gravitational acceleration, δ is the Kronecker delta function, $\mathcal{S}_{ij} = \Pi_{ij} - \tau_{ij}$ is the total ensemble-averaged stress tensor, Π_{ij} is the ensemble-averaged fluid stress and τ_{ij} is the Reynolds stress. For an incompressible fluid, the net ensemble-averaged fluid stress, composed of the pressure contribution p plus the viscous stress σ_{ij} , is defined by $\Pi_{ij} = -p\delta_{ij} + \sigma_{ij}$. In a Newtonian fluid, we may assume that $\sigma_{ij} = 2\mu e_{ij}$, where $e_{ij} = 1/2(\partial u_i/\partial x_j^* + \partial u_j/\partial x_i^*)$ is the strain rate tensor and μ is the dynamic viscosity. Although there is no universal model for τ_{ij} , even in the case of a single-phase flow, we use the common eddy viscosity approach to relate the anisotropic part of the Reynolds stress, τ_{ij}^{dev} , to the rate of strain, e_{ij} as $\tau_{ij}^{dev} \equiv \tau_{ij} - \frac{\delta_{ij}}{3} \tau_{kk} = -2\rho_0(\nu_t)_j e_{ij}$. Here, $(\nu_t)_j$ is the turbulent eddy viscosity in the j direction (j is not a free index here), obtained from an appropriate turbulence model. If grid resolution in the horizontal directions is considerably different from that in the vertical direction, the horizontal turbulent eddy viscosity $(\nu_t)_x = (\nu_t)_y$ may be different from that in the vertical direction $(\nu_t)_z$.

The governing Eqs. (3) and (4) are next transformed into the σ -coordinate system (see Fig. 1), which is given by

$$t = t^* \quad x = x^* \quad y = y^* \quad \sigma = \frac{z^* + h}{D} \quad (5)$$

where $D = h + \eta$ is the total water depth, h is the still water depth, and η is a free surface elevation. In the case of a multi-valued surface, however, the definition of a free surface elevation is arbitrary, and, we assume η is sufficiently smooth to be considered as a single-valued mean air-water interface.

Each term of (3) and (4) is transformed into the σ -coordinate system by multiplying by D and using chain differentiation rule as

$$\begin{aligned} D \frac{\partial \psi}{\partial x_j^*} &= D \frac{\partial \psi}{\partial x_j} \lambda_j + D \frac{\partial \psi}{\partial \sigma} \sigma_{x_j^*} \\ &= \frac{\partial D \psi}{\partial x_j} \lambda_j + \left(-\frac{D_{x_j}}{D} \lambda_j \right) D \psi + \left(\sigma_{x_j^*} \right) \frac{\partial D \psi}{\partial \sigma} \\ &= \frac{\partial D \psi}{\partial x_j} \lambda_j + \frac{\partial \sigma_{x_j^*} D \psi}{\partial \sigma}, \end{aligned} \quad (6)$$

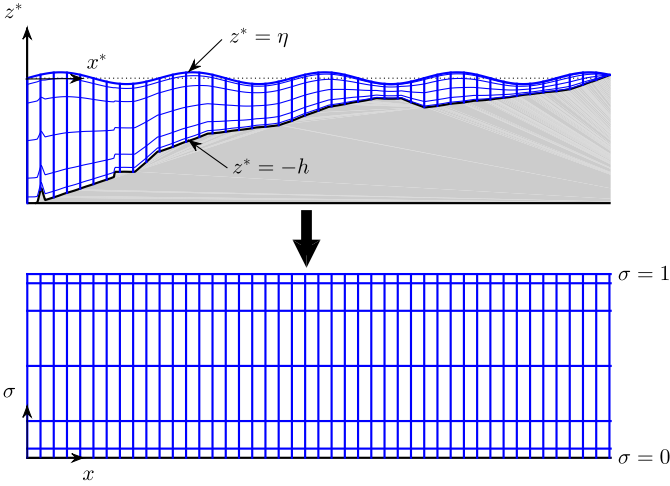


Fig. 1. Illustration of σ -coordinate transformation. The irregular physical domain in the (x^*, y^*, z^*, t^*) space is transformed to a rectangular computational domain in the (x, y, σ, t) space by an algebraic mapping. Here, only the mapping in the (x^*, z^*) -plane is shown. In both the y^* - and y -direction, the grid is uniform and is not plotted.

where $\lambda_j = 1 - \delta_{3j}$, $\partial(\cdot)/\partial t^* = (\cdot)_{t^*}$, $\partial(\cdot)/\partial x_j^* = (\cdot)_{x_j^*}$; hereafter summation inside expressions involving λ_j is not implied. Multiplying (3) by D and using (6), the continuity equation in the σ coordinates can be written as

$$\frac{\partial D}{\partial t} + \frac{\partial U_i}{\partial x_i} \lambda_i + \frac{\partial \Omega}{\partial \sigma} = 0. \quad (7)$$

where

$$U_i = D u_i,$$

$$\Omega = D(\sigma_{t^*} + \sigma_{x_j^*} u_j) = D\sigma_{t^*} + \sigma_{x_j^*} U_j. \quad (8)$$

Multiplying (4) by D and using (6), after doing some algebra, the complete and conservative well-balanced form of the ensemble-averaged momentum equation in the σ -coordinate system reads as

$$\begin{aligned} \frac{\partial U_i}{\partial t} + \frac{\partial}{\partial x_j} \left(U_i U_j / D + [gh\eta + g\eta^2/2] \delta_{ij} \right) \lambda_j + \frac{\partial U_i \Omega / D}{\partial \sigma} = \\ - \frac{1}{\rho_0} \left\{ D \frac{\partial p^h}{\partial x_i} \Big|_{\sigma=1} - \rho_0 g \eta h_{x_i} \right\} \lambda_i \quad (\text{barotropic pressure terms}) \\ - \frac{1}{\rho_0} \left\{ \frac{\partial \mathcal{P}}{\partial x_i} \lambda_i + \frac{\partial \sigma_{x_i^*} \mathcal{P}}{\partial \sigma} \right\} \quad (\text{dynamic pressure terms}) \\ + \frac{\partial 2(v_{eff})_j \mathcal{E}_{ij}}{\partial x_j} \lambda_j + \frac{\partial 2\sigma_{x_j^*} (v_{eff})_j \mathcal{E}_{ij}}{\partial \sigma} \quad (\text{diffusion terms}), \quad (9) \end{aligned}$$

where $(v_{eff})_n = v + (v_t)_n$, $n = 1, 2, 3$, and

$$\begin{aligned} \mathcal{P} = D \left(p^d + \frac{1}{3} \tau_{kk} \right) = D \left(p^d + \frac{2}{3} \rho_0 k \right) \\ \mathcal{E}_{ij} = D e_{ij} = \frac{1}{2} \left\{ \frac{\partial U_i}{\partial x_j} \lambda_j + \frac{\partial U_j}{\partial x_i} \lambda_i + \frac{\partial}{\partial \sigma} \left(\sigma_{x_j^*} U_i + \sigma_{x_i^*} U_j \right) \right\}. \quad (10) \end{aligned}$$

where k is the ensemble-averaged turbulent kinetic energy. Here, the total pressure is divided into the dynamic pressure $p^d = p - p^h$, and the hydrostatic pressure given by $\partial p^h / \partial \sigma = -D\rho_0 g$. Thus $p^h = \rho_0 g D(1 - \sigma) + p_a$ and $p^h \Big|_{\sigma=1} = p_a$, where p_a is the imposed air pressure at the free surface. Note that the dynamic pressure and diffusion terms in (9) and (10) are given in a conservative form as opposed to those given in the existing comparable formulations, such as Lin and Li (2002, equations 14–16,19) and Ma et al. (2012, equations 6,9,10).

2.2. Scalar transport equation

Following the same procedure as we did for the transformation of the momentum equation, the conservative form of the scalar transport equation in the σ -coordinate system can be written as

$$\begin{aligned} \frac{\partial \mathcal{C}}{\partial t} + \frac{\partial \mathcal{C} U_j / D}{\partial x_j} \lambda_j + \frac{\partial}{\partial \sigma} \left(\mathcal{C} [\Omega / D + \sigma_{x_j^*} w_c \delta_{3j}] \right) = \\ + \frac{\partial v_j \mathcal{D}_j}{\partial x_j} \lambda_j + \frac{\partial \sigma_{x_j^*} v_j \mathcal{D}_j}{\partial \sigma} + D \Gamma_{\langle c \rangle}. \quad (11) \end{aligned}$$

where $v_n = v + (v_t / \sigma_{\langle c \rangle})_n$, $\sigma_{\langle c \rangle}$ is the corresponding Schmidt number, $\mathcal{C} = D \langle c \rangle$, and $\mathcal{D}_j = (\partial \mathcal{C} / \partial x_j) \lambda_j + \partial \sigma_{x_j^*} \mathcal{C} / \partial \sigma$. Here, $\Gamma_{\langle c \rangle}$ represents the associated source/sink terms for $\langle c \rangle$, and w_c is a settling or rising velocity of $\langle c \rangle$, equal to zero for a neutrally buoyant quantity. For the case of negligibly small surface and bottom slopes ($\nabla_h h$ and $\nabla_h \eta \approx 0$), Eq. (11) simplifies to the expression given in Ma et al. (2013, 2014).

2.3. Turbulence model

An appropriate turbulence model is needed to estimate v_t as well as to provide the bulk turbulence statistics such as the ensemble-averaged turbulent kinetic energy and dissipation rate. In many numerical approaches, depending on the grid size in the vertical and horizontal directions, the corresponding eddy viscosity for the vertical direction, $v_t^v = (v_t)_3$, and horizontal directions, $v_t^h = (v_t)_{1,2}$, may not be of the same order. Here, we assume the more physically reasonable formulation $v_t = v_t^v = v_t^h$.

The Smagorinsky subgrid and $k - \epsilon$ models are commonly used turbulence models, depending on the grid resolution. The constant Smagorinsky model reads as $v_t = \frac{(c_s \Delta)^2}{D} \sqrt{2 \mathcal{E}_{ij} \mathcal{E}_{ij}}$, where Δ is the length scale on the order of the grid size, and $c_s \sim 0.1 - 0.2$ is the only input parameter. Having relatively larger grid sizes, which is usually the case in non-hydrostatic modeling using a few vertical σ -levels, a $k - \epsilon$ turbulence model is more appropriate to estimating v_t as below

$$v_t = c_\mu \frac{k^2}{\epsilon} = c_\mu \frac{\mathcal{K}^2}{D \mathcal{E}}, \quad (12)$$

where c_μ (Rodi, 1980) is an empirical coefficient, k is the ensemble-averaged turbulent kinetic energy, and ϵ is the ensemble-averaged turbulent dissipation rate. Transport equations for \mathcal{K} and \mathcal{E} need to be solved. The transport equation for \mathcal{K} and \mathcal{E} can be simply obtained by replacing \mathcal{C} in (11) by \mathcal{K} and \mathcal{E} respectively, where

$$D \Gamma_{\mathcal{K}} = \mathcal{P}_s - \mathcal{E}, \quad D \Gamma_{\mathcal{E}} = \frac{\mathcal{E}}{\mathcal{K}} [c_{1\mathcal{E}} \mathcal{P}_s - c_{2\mathcal{E}} \mathcal{E}]. \quad (13)$$

In the standard $k - \epsilon$ model (Rodi, 1980), we have $c_\mu = 0.09$, $c_{1\mathcal{E}} = 1.44$, $c_{2\mathcal{E}} = 1.92$, $\sigma_{\mathcal{K}} = 1.0$ and $\sigma_{\mathcal{E}} = 1.3$. Using the RNG approach with scale expansions for the Reynolds stress and production of dissipation terms, Yakhot et al. (1992) derived a dynamic procedure to determine $c_{2\mathcal{E}}$ as

$$c_{2\mathcal{E}} = 1.68 + \frac{c_\mu \zeta^3 (1 - \zeta / 4.38)}{1 + 0.012 \zeta^3}, \quad (14)$$

where $\zeta = \frac{\mathcal{K}}{D \mathcal{E}} \sqrt{2 \mathcal{E}_{ij} \mathcal{E}_{ij}}$ is the ratio of the turbulent and mean strain time scales. The rest of the closure coefficients are given by $c_\mu = 0.085$, $c_{1\mathcal{E}} = 1.42$, and $\sigma_{\mathcal{K}} = \sigma_{\mathcal{E}} = 0.72$. Finally, the rate of shear production \mathcal{P}_s is given by

$$\mathcal{P}_s = -\tau_{ij} \left[\frac{\partial U_i}{\partial x_j} \lambda_j + \frac{\partial \sigma_{x_j^*} U_i}{\partial \sigma} \right], \quad (15)$$

where the Reynolds stress τ_{ij} may be estimated using a linear model given by $\tau_{ij} = \frac{\delta_{ij}}{3} \tau_{kk} - 2\rho_0 (v_t)_j e_{ij}$ or a nonlinear model as in Ma et al. (2013).

3. Surface and bottom boundary conditions

The free surface and the bottom may be expressed as $F = z^* - \xi = 0$ where $\xi = \eta$ at the free surface ($\sigma = 1$), and $\xi = -h$ at the bottom ($\sigma = 0$). We define the local coordinate system $(\mathbf{x}'_1, \mathbf{x}'_2, \mathbf{x}'_3)$, such that \mathbf{x}'_3 is the vector normal to the surface oriented in the $+z^*$ sense, $F = 0$, given by

$$\mathbf{x}'_3 = \frac{\nabla F}{|F|} = \frac{1}{A}(-\xi_{x'_1}, -\xi_{x'_2}, 1) = \frac{1}{A}(-\xi_x, -\xi_y, 1), \quad (16)$$

where $A = |F| = \sqrt{1 + \xi_x^2 + \xi_y^2}$. The other two unit vectors can be any orthogonal pair of vectors ($\mathbf{x}'_1 \cdot \mathbf{x}'_2 = 0$) in the plane tangent to the $F = 0$ surface. Here, we choose

$$\begin{aligned} \mathbf{x}'_1 &= \frac{1}{B}(1, 0, \xi_x), & B &= \sqrt{1 + \xi_x^2} \\ \mathbf{x}'_2 &= \mathbf{x}'_3 \times \mathbf{x}'_1 = \frac{1}{AB}(-\xi_x \xi_y, 1 + \xi_x^2, \xi_y). \end{aligned} \quad (17)$$

The transformation of any vector, $\boldsymbol{\varphi}$, in the Cartesian coordinates into the local coordinates, $\boldsymbol{\varphi}'$, on $F = 0$ is given by

$$\boldsymbol{\varphi}'_j = \mathbf{C}_{ij} \varphi_i, \quad \mathbf{C} = \begin{bmatrix} \frac{1}{B} & \frac{-\xi_x \xi_y}{AB} & \frac{-\xi_x}{A} \\ 0 & \frac{1 + \xi_x^2}{AB} & \frac{-\xi_y}{A} \\ \frac{\xi_x}{B} & \frac{\xi_y}{AB} & \frac{1}{A} \end{bmatrix}, \quad (18)$$

where \mathbf{C}_{ij} is the cosine of the angle between the \mathbf{x}^*_i and \mathbf{x}'_j axes. In addition, the transformation of any tensor in Cartesian coordinates into the local coordinates on $F = 0$ is given by

$$\varphi'_{mn} = \mathbf{C}_{im} \mathbf{C}_{jn} \varphi_{ij}. \quad (19)$$

3.1. Kinematic boundary conditions

Assuming no mass flux at the interface, a particle initially on the interface will remain on the interface in which we can write $DF/Dt^* = \partial F/\partial t^* + u_j \partial F/\partial x^*_j = 0$. Thus, the kinematic surface and bottom boundary conditions in the σ coordinates are simply written as

$$W \Big|_{\sigma=0,1} = D\xi_t + \xi_x U \Big|_{\sigma=0,1} + \xi_y V \Big|_{\sigma=0,1}, \quad (20)$$

where $\xi = \eta$ at the free surface ($\sigma = 1$), and $\xi = -d$ at the bottom ($\sigma = 0$). Because $\sigma_{t^*} \Big|_{\sigma=0,1} = -\xi_t/D$, $\sigma_{x^*_1} \Big|_{\sigma=0,1} = -\xi_x/D$, and $\sigma_{x^*_2} \Big|_{\sigma=0,1} = -\xi_y/D$, we have

$$\begin{aligned} \Omega \Big|_{\sigma=0,1} &= D\sigma_{t^*} \Big|_{\sigma=0,1} + \sigma_{x^*_j} \Big|_{\sigma=0,1} U_j \Big|_{\sigma=0,1} = 0 \\ \frac{\partial \Omega}{\partial \sigma} \Big|_{\sigma=0,1} &= -\frac{\xi_x}{D} \frac{\partial U}{\partial \sigma} \Big|_{\sigma=0,1} - \frac{\xi_y}{D} \frac{\partial V}{\partial \sigma} \Big|_{\sigma=0,1} + \frac{1}{D} \frac{\partial W}{\partial \sigma} \Big|_{\sigma=0,1} = 0. \end{aligned} \quad (21)$$

Thus in the σ coordinates, the surface and bottom vertical velocity as well as vertical acceleration are always zero.

3.2. Tangential stress boundary conditions

Using (19), the transformed total stress on $F = 0$ is given by

$$\mathcal{S}'_{3i} \Big|_{\sigma=0,1} = \mathbf{C}_{ji} \left(-\frac{\xi_x}{A} \mathcal{S}_{1j} - \frac{\xi_y}{A} \mathcal{S}_{2j} + \frac{1}{A} \mathcal{S}_{3j} \right) \Big|_{\sigma=0,1}, \quad (22)$$

where $\mathcal{S}_{ij} = \mathcal{S}^p \delta_{ij} + \mathcal{S}^v_{ij}$ is the total stress including the pressure, $\mathcal{S}^p = -(p^h + \mathcal{P}/D)$, and viscous stress $\mathcal{S}^v_{ij} = 2\rho_0(\nu_{eff})_j(\mathcal{E}_{ij}/D)$ contributions.

If the state of stress in the external media is available, the continuity of the tangential stress on $F = 0$ reads as

$$\mathcal{S}'_{3i} \Big|_{\sigma=0,1} = \mathcal{S}'_{3i}{}^{ext} \Big|_{\sigma=0,1}, \quad (23)$$

where $i = (1, 2)$, and $\mathcal{S}'_{3i}{}^{ext} \Big|_{\sigma=0,1}$ is the external stress on $F = 0$ in the i direction, e.g., the wind stress parallel to the free surface or the bottom shear stress. Here, $(\)$ represent the local coordinate system given by (16). However, if the external media is assumed to be rigid, $\mathcal{S}'_{3i}{}^{ext} \Big|_{\sigma=0,1}$ is replaced by the estimated shear stress near the rigid boundary, as discussed below.

Multiplying (23) by D and using (22), and assuming the same turbulent eddy viscosity in all directions on $F = 0$, we obtain

$$\begin{aligned} -\xi_x[\mathcal{E}_{11} - \mathcal{E}_{33}] + [1 - \xi_x^2]\mathcal{E}_{13} - \xi_y[\mathcal{E}_{12} + \xi_x \mathcal{E}_{23}] &= \frac{AD}{2\rho_0 \nu_{eff}} \mathcal{F}_1^{ext} \Big|_{\sigma=0,1} \\ -\xi_y[\mathcal{E}_{22} - \mathcal{E}_{33}] + [1 - \xi_y^2]\mathcal{E}_{23} - \xi_x[\mathcal{E}_{12} + \xi_y \mathcal{E}_{13}] &= \frac{AD}{2\rho_0 \nu_{eff}} \mathcal{F}_2^{ext} \Big|_{\sigma=0,1}, \end{aligned} \quad (24)$$

where

$$\begin{aligned} \mathcal{F}_1^{ext} &= B \mathcal{S}'_{31}{}^{ext} \\ \mathcal{F}_2^{ext} &= \frac{\xi_x \xi_y}{B} \mathcal{S}'_{31}{}^{ext} + \frac{A}{B} \mathcal{S}'_{32}{}^{ext}. \end{aligned} \quad (25)$$

Rearranging (24), the condition of continuity of the tangential stress on $F = 0$ finally gives

$$\begin{aligned} \frac{\partial U}{\partial \sigma} \Big|_{\sigma=0,1} &= \frac{D^2}{A\rho_0 \nu_{eff}} \mathcal{F}_1^{ext} \Big|_{\sigma=0,1} - \xi_x \frac{\partial W}{\partial \sigma} \Big|_{\sigma=0,1} \\ &+ \frac{D}{A^2} \left\{ 2\xi_x(U)_x - [1 - \xi_x^2](W)_x + \xi_y[(U)_y + (V)_x + \xi_x(W)_y] \right\} \Big|_{\sigma=0,1} \\ \frac{\partial V}{\partial \sigma} \Big|_{\sigma=0,1} &= \frac{D^2}{A\rho_0 \nu_{eff}} \mathcal{F}_2^{ext} \Big|_{\sigma=0,1} - \xi_y \frac{\partial W}{\partial \sigma} \Big|_{\sigma=0,1} \\ &+ \frac{D}{A^2} \left\{ 2\xi_y(V)_y - [1 - \xi_y^2](W)_y + \xi_x[(V)_x + (U)_y + \xi_y(W)_x] \right\} \Big|_{\sigma=0,1}, \end{aligned} \quad (26)$$

where

$$\begin{aligned} (U)_x &= \partial U_i / \partial x - U_i D_x / D = D \frac{\partial u_i}{\partial x} \\ (U)_y &= \partial U_i / \partial y - U_i D_y / D = D \frac{\partial u_i}{\partial y}. \end{aligned} \quad (27)$$

If we only consider the wind stress at the free surface, using (22) we have

$$\begin{aligned} \mathcal{F}_1^{ext} \Big|_{\sigma=1} &= \frac{1}{A} \left\{ (1 - \xi_x^2) \tau_{wx} - \xi_x \xi_y \tau_{wy} \right\} \\ \mathcal{F}_2^{ext} \Big|_{\sigma=1} &= \frac{1}{A} \left\{ (1 - \xi_y^2) \tau_{wy} - \xi_x \xi_y \tau_{wx} \right\}, \end{aligned} \quad (28)$$

where τ_{wx} and τ_{wy} are the wind stresses in the x and y directions, respectively. In the case of negligibly small wind speeds, $\mathcal{F}_1^{ext} \Big|_{\sigma=1} = \mathcal{F}_2^{ext} \Big|_{\sigma=1} = 0$.

At the bottom, the external shear stress parallel to the bottom, or bottom stress, can be estimated from the law of the wall as

$$\mathcal{S}'_{31}{}^{ext} \Big|_{\sigma=0} \approx \rho_0 u_*^2 \frac{U'_b}{U'_b}, \quad \mathcal{S}'_{32}{}^{ext} \Big|_{\sigma=0} \approx \rho_0 u_*^2 \frac{V'_b}{U'_b}, \quad (29)$$

where $U'_b = \sqrt{U'^2 + V'^2} \Big|_{\sigma=\Delta\sigma_1/2}$ is the magnitude of velocity parallel to the bed at the first grid cell above the bed. Using (18), U' and V' , the horizontal velocities (velocity times D) parallel to the bed,

are given by

$$U' = \mathbf{C}_{j1}U_j = \frac{1}{B} \left(U - h_x W \right) \Big|_{\sigma=\Delta\sigma_{1/2}}$$

$$V' = \mathbf{C}_{j2}U_j = \frac{1}{AB} \left(-h_x h_y U + [1 + h_x^2]V - h_y W \right) \Big|_{\sigma=\Delta\sigma_{1/2}}, \quad (30)$$

and u_* is the friction velocity given by

$$u_* = \frac{\kappa \beta U'_b}{D \ln(z_b/z_0)}, \quad (31)$$

where $\kappa = 0.41$ is the Van Karman constant, and $\beta \leq 1$ represents the stratification effects in the bottom boundary layer. Here, z_b and z_0 are the distances from the bed at which the ensemble-averaged velocities parallel to the bed are assumed to be U'_b/D and zero respectively, depending on the boundary layer characteristics as well as the roughness length-scale, k_s . For a fully rough turbulent boundary layer, it is typically assumed that $z_0 = k_s/30$.

3.3. Normal stress boundary condition

If the state of stress in the external media is available, the continuity of the normal stress reads as

$$D \mathcal{S}'_{33} \Big|_{\sigma=0,1} = \left\{ - \left(D p^h + \mathcal{P} \right) + \frac{2\rho_0 v_{eff}}{A^2} \left(\xi_x^2 \mathcal{E}_{11} + \xi_y^2 \mathcal{E}_{22} + \mathcal{E}_{33} + 2\xi_x \xi_y \mathcal{E}_{12} - 2\xi_x \mathcal{E}_{13} - 2\xi_y \mathcal{E}_{23} \right) \right\}_{\sigma=0,1} = D \mathcal{S}'_{33} \Big|_{\sigma=0,1}^{ext} \quad (32)$$

where the normal stress in the local coordinate, $\mathcal{S}'_{33} \Big|_{\sigma=0,1}$, is obtained using (22). Rearranging (32), we have

$$\mathcal{P} \Big|_{\sigma=0,1} = -D \left(p^h \Big|_{\sigma=0,1} + \mathcal{S}'_{33} \Big|_{\sigma=0,1}^{ext} \right) - \frac{\rho_0 v_{eff}}{A^2} \left\{ 2\xi_x [(W)_x - \xi_x (U)_x] + 2\xi_y [(W)_y - \xi_y (V)_y] - 2\xi_x \xi_y [(U)_y + (V)_x] \right\}_{\sigma=0,1} \quad (33)$$

Neglecting viscous stresses in the air side, we have $\mathcal{S}'_{33} \Big|_{\sigma=1}^{ext} = -p_a$ on the free surface. The atmospheric pressure, p_a , is absorbed in the hydrostatic pressure. Thus, the Dirichlet-type boundary condition for the modified dynamic pressure reads as

$$\mathcal{P} \Big|_{\sigma=1} = - \frac{\rho_0 v_{eff} \Big|_{\sigma=1}}{A^2} \left\{ 2\xi_x [(W)_x - \xi_x (U)_x] + 2\xi_y [(W)_y - \xi_y (V)_y] - 2\xi_x \xi_y [(U)_y + (V)_x] \right\}_{\sigma=1}. \quad (34)$$

At the bottom, however, such a relation can not be applied unless the bottom is a dynamically coupled layer. In the case of a rigid bottom, using the vertical momentum equation we can write

$$\frac{\partial \mathcal{P}}{\partial \sigma} \Big|_{\sigma=0} = -D\rho_0 \left\{ \frac{\partial W}{\partial t} + \frac{\partial WU/D}{\partial x} + \frac{\partial WV/D}{\partial y} + \frac{\partial W\Omega/D}{\partial \sigma} \right\}_{\sigma=0} + D\rho_0 \left\{ \frac{\partial 2(v_{eff})_j \mathcal{E}_{3j}}{\partial x_j} \lambda_j + \frac{\partial 2\sigma_{x_j} (v_{eff})_j \mathcal{E}_{3j}}{\partial \sigma} \right\}_{\sigma=0}. \quad (35)$$

Neglecting the Reynolds stress gradients at the bottom and using (21), a Neumann-type boundary condition for the modified dy-

namic pressure at the bottom reads as

$$\frac{\partial \mathcal{P}}{\partial \sigma} \Big|_{\sigma=0} = -D\rho_0 \left\{ \frac{\partial W}{\partial t} + \frac{\partial WU/D}{\partial x} + \frac{\partial WV/D}{\partial y} \right\}_{\sigma=0}. \quad (36)$$

3.4. Neumann-type boundary condition for a scalar quantity

The Neumann boundary condition for a scalar quantity, $\langle c \rangle$, normal to the interface, $F = 0$, may be expressed as

$$\frac{\partial \langle c \rangle}{\partial x'_3} \Big|_{\sigma=0,1} = \langle f \rangle \Big|_{\sigma=0,1}, \quad (37)$$

where $\langle f \rangle \Big|_{\sigma=0,1}$ represent the corresponding ensemble-averaged flux of $\langle c \rangle$ across the interface. In the case of $\langle f \rangle \Big|_{\sigma=0,1} = 0$, (37) is called a zero-gradient boundary condition for $\langle c \rangle$ on the interface, commonly used for passive scalars such as salinity, the turbulent kinetic energy, and dissipation rate. Multiplying (37) by D and using (16), we have

$$D \frac{\partial \langle c \rangle}{\partial x'_3} \Big|_{\sigma=0,1} = D(\nabla \langle c \rangle) \Big|_{\sigma=0,1} \cdot \mathbf{x}'_3 = D \frac{\partial \langle c \rangle}{\partial x'_j} \Big|_{\sigma=0,1} x'_{3j} = \mathcal{F} \Big|_{\sigma=0,1}. \quad (38)$$

where $\mathcal{F} \Big|_{\sigma=0,1} = D \langle f \rangle \Big|_{\sigma=0,1}$. Using (6), the Neumann-type boundary condition for $\mathcal{C} = D \langle c \rangle$ normal to the interface on $F = 0$ can be written as

$$\frac{\partial \mathcal{C}}{\partial \sigma} \Big|_{\sigma=0,1} = \left\{ \frac{D}{A} \mathcal{F} + \frac{D^2}{A^2} \left(\xi_x \frac{\partial \mathcal{C}/D}{\partial x} + \xi_y \frac{\partial \mathcal{C}/D}{\partial y} \right) \right\}_{\sigma=0,1}. \quad (39)$$

3.5. Boundary conditions for \mathcal{K} and \mathcal{E}

A zero-gradient boundary condition, $\mathcal{F} = 0$, is imposed for both \mathcal{K} and \mathcal{E} at $\sigma = 1$, and $\partial \mathcal{K}/\partial \sigma$ and $\partial \mathcal{E}/\partial \sigma$ at $\sigma = 1$ are estimated using (39).

The Dirichlet-type boundary conditions for both \mathcal{K} and \mathcal{E} is used near the bottom, given by

$$\mathcal{K}_b = D \frac{u_*^2}{\sqrt{c_\mu}}, \quad \mathcal{E}_b = D \frac{u_*^3}{\kappa z_b} \quad (40)$$

where κ is the Von Karman constant, z_b is the distance from the bed, and u_* is a friction velocity given by (31). Strictly speaking, this is based on the mixing length assumption and the simplified k -equation (turbulence production equals to dissipation) for a steady boundary layer.

4. The role of surface slopes in the near-surface velocity and turbulence fields

In this section, model results for the time-averaged velocity field in a deep-water standing wave in a closed basin as well as the free surface evolution, velocity and turbulent kinetic energy in surf zone regular spilling breaking waves are compared with those predicted by the original version of NHWAVE (Ma et al., 2012) and the corresponding measurements of Ting and Kirby (1994). In the original model, the dynamic boundary conditions described in the previous section have been simplified by the neglect of the terms which include the surface or bottom slopes. Derakhti et al. (2015) show that the new boundary conditions and numerical schemes are not rotationally biased in the (x, y) plane.

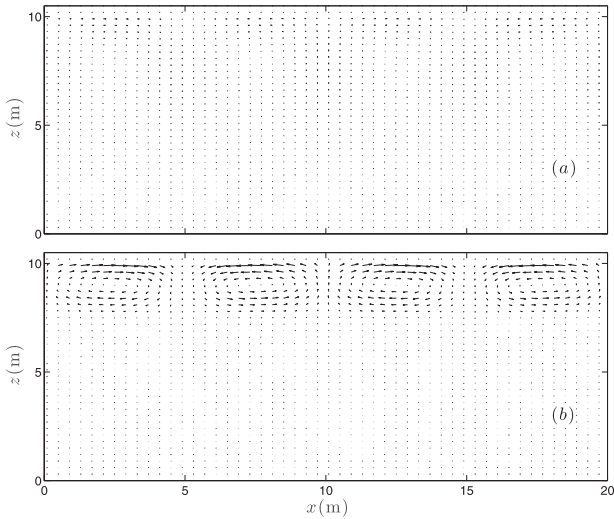


Fig. 2. Spatial distribution of the long-time-averaged velocity field in a standing wave in a closed basin. Comparison between NHWAVE results with 10 vertical σ -levels using the (a) consistent and (b) simplified boundary conditions.

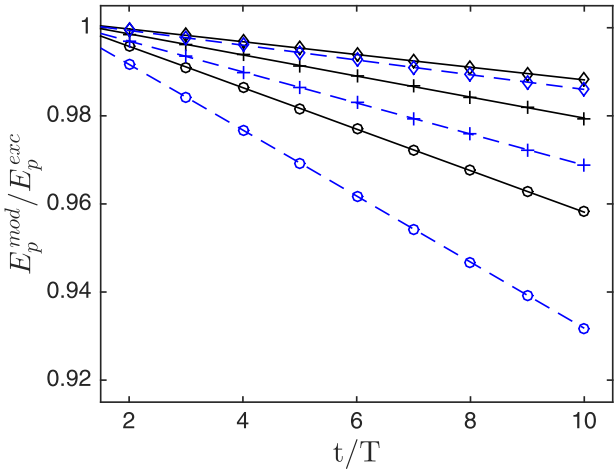


Fig. 3. Time variation of the normalized wave-averaged potential energy of a standing wave in a closed basin. Comparison between NHWAVE results with (circle symbols) 3, (+ symbols) 5 and (diamonds symbols) 10 vertical σ -levels using the (solid lines) consistent and (dashed lines) simplified boundary conditions.

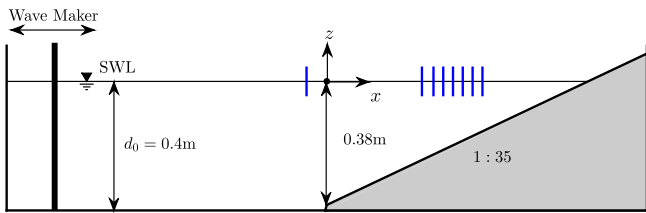


Fig. 4. Experimental layout of Ting and Kirby (1994). Vertical solid lines: the cross-shore locations of the velocity measurements.

4.1. Standing wave in a closed basin

Using the simplified velocity boundary condition, e.g., $\partial u / \partial \sigma = 0$, imposes an unphysical source of vorticity at the free surface in the case of a non-zero horizontal gradient of the vertical velocity, $\partial w / \partial x \neq 0$, generating an unphysical circulation pattern. A deep-water standing wave in a closed basin, with length of $L = 20$ m and depth of $h = 10$ m, is selected to examine this effect. The initial surface elevation is $\eta_0 = a \cos kx$, where $k = 2\pi / L$, $a = 0.1$ m is the

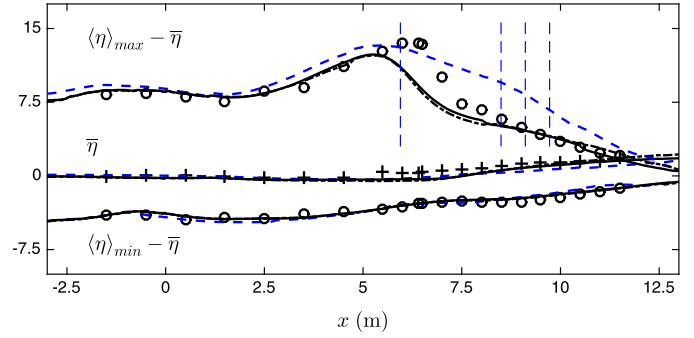


Fig. 5. Cross-shore distribution of crest and trough elevations as well as mean water level for the surf zone spilling breaking case of Ting and Kirby (1994). Comparison between NHWAVE results with 10 vertical σ -levels using the new model with RNG-based $k - \epsilon$ (solid lines), standard $k - \epsilon$ (dotted-dashed lines), and the original model (blue dashed lines) and the corresponding measurements of Ting and Kirby (1994) (markers). Vertical dashed lines are the cross-shore locations of the results shown in Fig. 6.

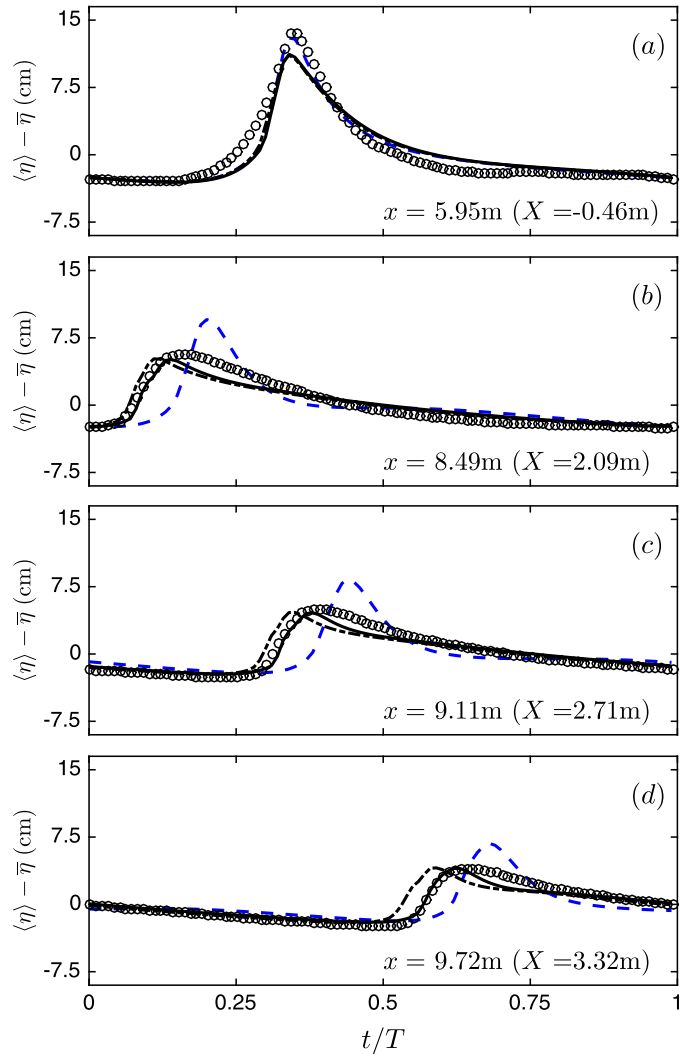


Fig. 6. Phase-averaged free surface elevations for the surf zone spilling breaking case at different cross-shore locations shown in Fig. 5. Definitions are the same as in Fig. 5. Here, $X = x - x_b$, is the horizontal distance from the break point.

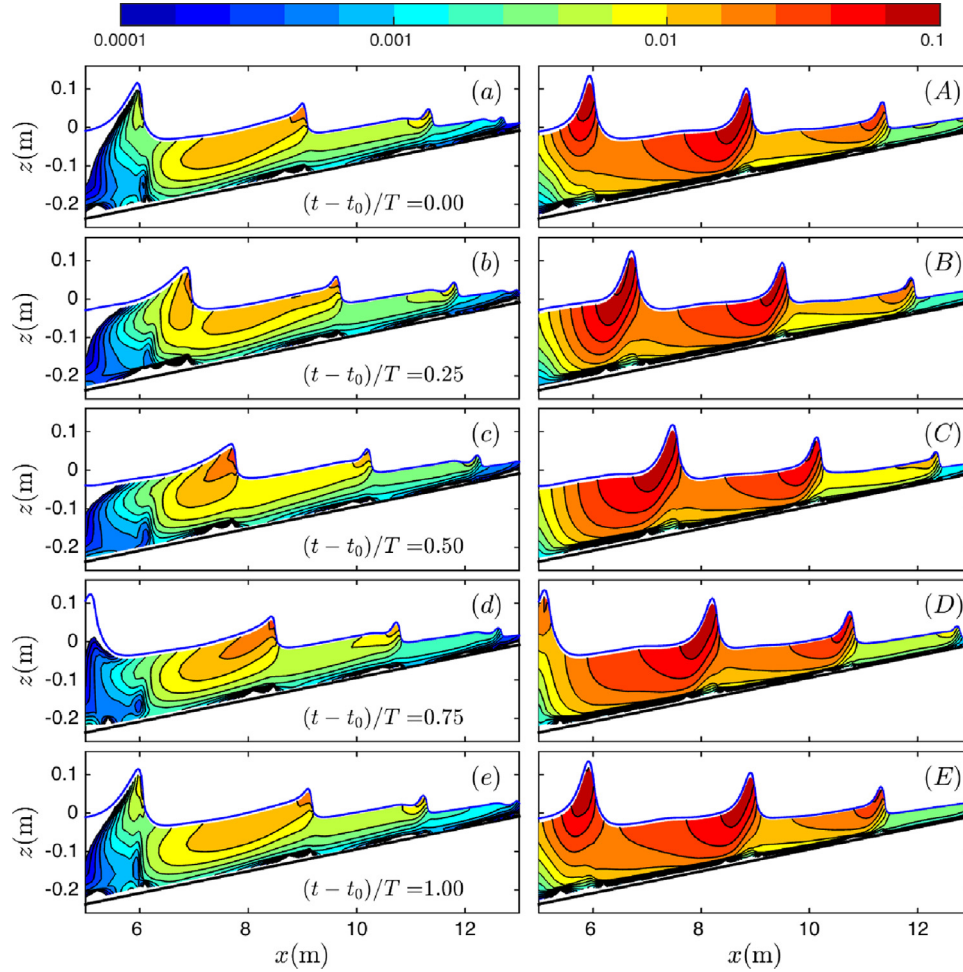


Fig. 7. Snapshots of the turbulent kinetic energy, $k(\text{m}^2/\text{s}^2)$, distribution for the surf zone spilling breaking case. Comparison between NHWAVE results with 10 vertical σ -levels using the (a–e) new model with RNG-based $k-\epsilon$ and (A–E) original model.

amplitude of the standing wave and L is the wave length, equals to the basin's length. Since $kh = \pi$, it is a relatively short wave. Based on the linear dispersion relation, the wave period is equal to $T = 3.59$ s. A uniform grid spacing of 0.2 m in the horizontal direction, and 10 constant σ levels are used. The simulation time is 36.0 s, about 10 wave periods. To calculate a long-time averaged velocity field, the results are first interpolated onto an Eulerian grid of $\Delta z = 0.1$ m and $\Delta x = 0.2$ m, and then time averaging is performed over 10 wave periods. Fig. 2 shows the existence of an unphysical circulation pattern in the original model results using $\partial u / \partial \sigma = 0$ boundary conditions. Using linear theory, it can be shown that the magnitude of the instantaneous unphysical vorticity at the free surface is proportional to $(ka)T^{-1}$. In the deep water regime, it then becomes $ag^{-1}T^{-3}$, and increases with increasing wave height or decreasing wave period.

In addition, using the consistent boundary conditions, the potential energy loss is decreased compared with the linearized analytical solution, especially at cases with a few vertical σ -levels as shown in Fig. 3.

4.2. Surf zone regular breaking waves

The surf zone regular spilling breaking case of Ting and Kirby (1994) is selected here, to examine the role of surface slopes on the prediction of free surface evolution as well as wave-breaking-induced velocity and turbulence fields in the surf zone.

Fig. 4 sketches the experimental layout and the cross-shore locations of the available velocity measurements. This experiment has been widely used by other researchers to validate both non-hydrostatic models (Bradford, 2011; 2012; 2014; Smit et al., 2013; Ma et al., 2014) and VOF-based RANS models (Lin and Liu, 1998; Bradford, 2000; Ma et al., 2011).

A uniform grid of $\Delta x = 0.025$ m is used in the horizontal direction, and 10 σ levels are used in the vertical direction. At the left inflow boundary, the free surface location and velocities are calculated using the theoretical relations for Cnoidal waves given in Wiegel (1960). The numerical domain is extended beyond the maximum run-up, and the wetting/drying cells are treated as described in Ma et al. (2012, Section 3.4) by setting $D_{\min} = 0.001$ m. In this section, $\langle \rangle$ and $\overline{(\)}$ refer to phase and time averaging over five subsequent waves after the results reach quasi-steady state, respectively. The mean water depth is defined as $\bar{D} = h + \bar{\eta}$, where h is the still water depth and $\bar{\eta}$ is the wave set-down/set-up. As in Ting and Kirby (1994), $x = 0$ is the cross-shore location in which $h = 0.38$ m, and $X = x - x_b$ is the horizontal distance from the initial break point, x_b . In Ting and Kirby (1994), the break point for spilling breakers was defined as the location where air bubbles begin to be entrained in the wave crest ($x_b = 6.40$ m). In the model the break point is taken to be the cross-shore location at which the wave height starts to decrease.

Fig. 5 shows the cross-shore distribution of crest, $\langle \eta \rangle_{\max}$, and trough, $\langle \eta \rangle_{\min}$, elevations as well as mean water level, $\bar{\eta}$ in the

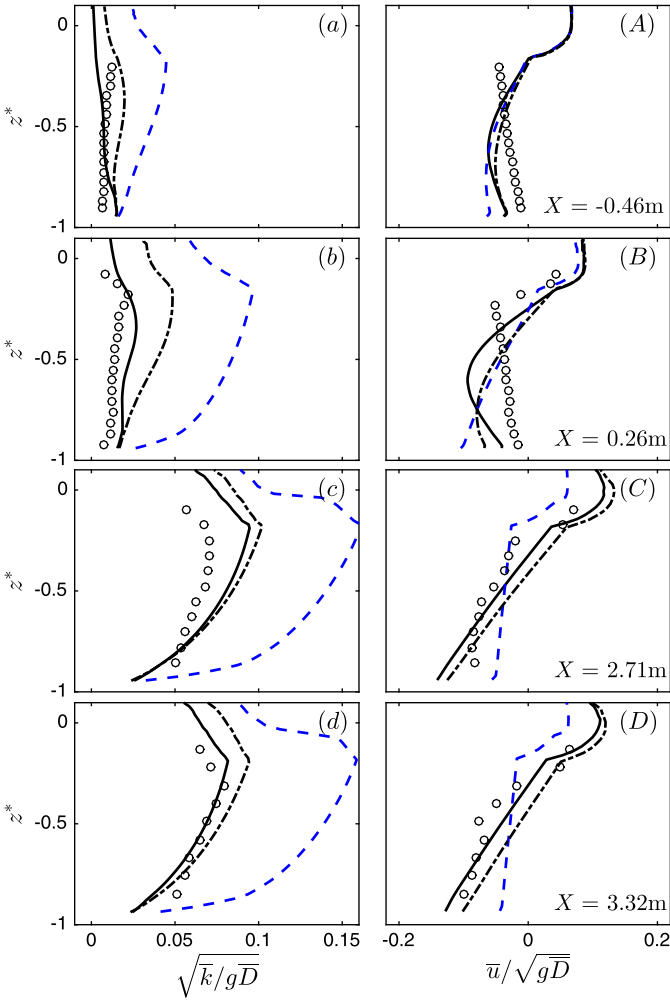


Fig. 8. Time-averaged normalized (a–d) turbulent kinetic energy, $\sqrt{k/g\bar{D}}$, and (A–D) horizontal velocity (undertow), $\bar{u}/\sqrt{g\bar{D}}$, profiles at different cross-shore locations close to the initial break point ($X = -0.46$ m, 0.26 m) and in the inner surf zone ($X = 2.71$ m, 3.32 m). Comparison between NHWAVE results with 10 vertical σ -levels using the new model with RNG-based $k-\epsilon$ (solid lines), standard $k-\epsilon$ (dotted-dashed lines), and the original model (blue dashed lines) and the corresponding measurements of Ting and Kirby (1994) (circle markers). Here, $\bar{D} = h + \bar{\eta}$, where h is the still water depth and $\bar{\eta}$ is the wave set-up/set-down.

shoaling, transition and inner surf zone regions predicted by the new and original model together with the corresponding measurements. In the shoaling zone, the new model accurately captures the water surface evolution compared with the observation. The predicted cross-shore location of the initial break point is approximately 0.7 m seaward of the observed one. In the transition region, $\langle \eta \rangle_{\max}$ is underpredicted by the new model compared with the measurement (see also Fig. 6a). Derakhti et al. (2016a) show that this early initiation of breaking and underprediction of $\langle \eta \rangle_{\max}$ in the transition region occur regardless of the choice of vertical resolution. The same trend has been reported in previous two-dimensional VOF/RANS studies of surf zone breaking waves; see, for example, Lin and Liu (1998, Figure 3a), Bradford (2000, Figure 1) and Ma et al. (2011, Figure 9). Typical vertical grid spacing near the breaking crest in those studies were approximately four times smaller than in the present study, suggesting that this discrepancy is not due to a selected numerical resolution or the single-valued free surface assumption imposed in the σ -coordinate system. The discrepancy is believed to be related to the limitation of the $k-\epsilon$ turbulence closure model in a rapidly distorted shear flow (Lin and Liu, 1998), which is the case in breaking waves.

In the inner surf zone, the new model predicts the water surface evolution with reasonable accuracy compared with observations. The original model, on the other hand, overpredicts $\langle \eta \rangle_{\max}$ in almost the entire surf zone (see also Ma et al. (2014, Figure 5)). Such overprediction of $\langle \eta \rangle_{\max}$ or wave heights in the surf zone also was reported in the σ -coordinate non-hydrostatic RANS simulations by Bradford (2012) and Bradford (2014). Those studies used the simplified surface boundary conditions, as in the original NHWAVE model, suggesting that neglecting the effect of surface slopes in the dynamic surface boundary conditions results in a significant underprediction of the total wave-breaking-induced energy dissipation in the surf zone. This observation is further discussed in the discussion section. Sawtooth-like waves in the inner surf zone are predicted fairly reasonably by the new model compared with observations, as shown in Fig. 6(b–d). However, the phase-averaged free surface elevations, $\langle \eta \rangle$, predicted by the original model deviate from the experimental data. Results show that using the RNG-based $k-\epsilon$ model gives a better estimation of the wave phase-speed compared with that predicted by the standard $k-\epsilon$ model. Using different $k-\epsilon$ models, however, has a negligibly small effect on the predicted wave height and wave set-up, in comparison to the corrections presented by consistent treatment of boundary conditions. Because the wave heights predicted by both the standard and RNG-based $k-\epsilon$ models are approximately the same, the larger apparent wave phase speed predicted by the standard $k-\epsilon$ model, shown in Fig. 6, must be related to the difference in the model prediction of wave-breaking-induced turbulence or mean current. We note that the slightly weaker undertow current predicted by the standard $k-\epsilon$ model compared with that by the RNG-based $k-\epsilon$ model, as shown in Fig. 8, can explain some part of the increase in the apparent wave phase speed. However, the question of how turbulence can affect the phase wave speed remains unexplained.

Fig. 7 shows that the structure of the turbulent kinetic energy, k , predicted by the new model is considerably different compared with that predicted by the original model. In addition, the k values predicted by the original model are much larger than those predicted by the new model. As shown in Lin and Liu (1998, Figures 12a and 13a), a roller region in the breaking wave front is a source region of turbulence generation, in which k values are relatively large. Thus, the structure of instantaneous k predicted by the new model is significantly improved compared to that predicted by the original model. The wrong location of high k regions predicted by the original model is mainly due to imposing $\partial u / \partial \sigma = 0$ boundary condition at the free surface, leading to a significant change of the production term at the bore-front region.

Fig. 8 (a–d) shows the time-averaged k values predicted by both the new and original models together with the corresponding measurements of Ting and Kirby (1994). It is seen that the original model (dashed lines) considerably overpredicts k in the entire surf zone compared with the experimental data. In addition, the RNG-based $k-\epsilon$ model (solid lines) gives a better estimation of k compared with the standard $k-\epsilon$ model (dashed-dotted lines), especially at the transition region. We also found that using the complete form of the diffusion terms in both the momentum and $k-\epsilon$ equations has an important role in the correct prediction of the k distribution inside the surf zone and prevents the unphysical continuous seaward propagation of the k patch as observed in the original model results.

Finally, Fig. 8(A–D) shows that both the vertical structure and magnitude of the predicted undertow current by the new model are more consistent with the corresponding measurements compared with those estimated by the original model. A relatively weak vertical gradient of the predicted undertow profiles by the original model shown in Fig. 8(C, D) (dashed lines) is due to the overprediction of the eddy viscosity ν_t as discussed in the

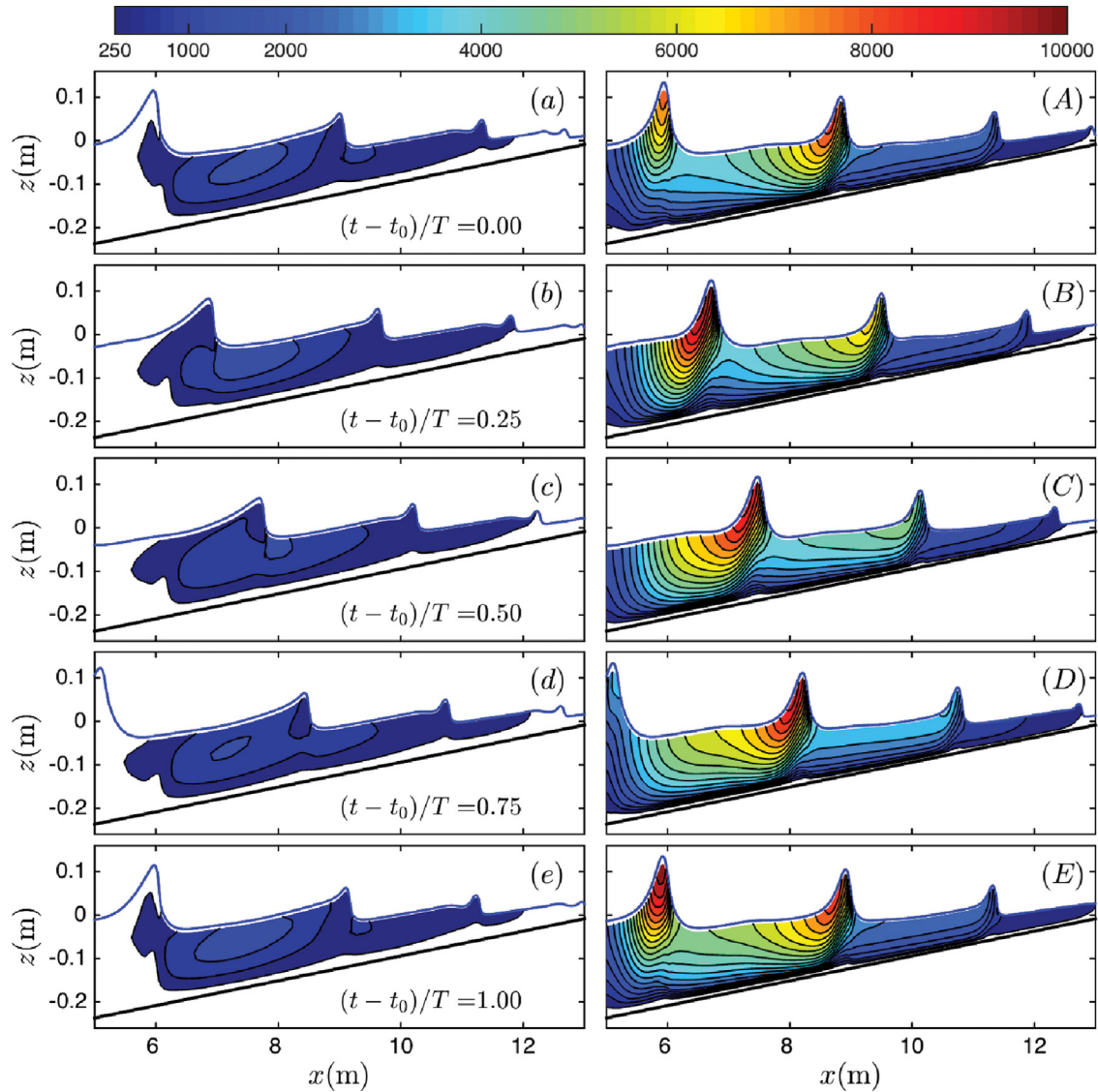


Fig. 9. Snapshots of the normalized turbulent eddy viscosity, v_t/v , distribution for the surf zone spilling breaking case. Comparison between NHWAVE results with 10 vertical σ -levels using the (a–e) new model with RNG-based $k-\epsilon$ and (A–E) original model. Contours are 250 to 9750 with interval of 500.

following section. We believe that such excessive vertical mixing resulted in the uniform predicted undertow profiles reported in Figures 12 and 13 of Bradford (2014), where the effect of surface slopes in the dynamic surface boundary conditions was ignored as in the original NHWAVE model.

5. Discussion

The standard estimation of surf zone eddy viscosity $v_t \approx 0.01\bar{D}\sqrt{g\bar{D}}$ (Svendensen, 1987) gives the normalized eddy viscosity v_t/v in the range of 500 ~ 2000 in the considered surf zone spilling case, which is consistent with that reported in Lin and Liu (1998) in the regions below the trough levels. Fig. 9 shows the snapshots of the spatial distribution of v_t/v predicted by the new (panels a–e) and original (panels A–E) models. The structure of the predicted v_t/v below the trough levels by the new model are consistent with that reported in the VOF/RANS simulation in Lin and Liu (1998, Figures 12c and 13c), where the magnitude of the new model predictions is up to 30% smaller than for the VOF/RANS simulation. Derakhti et al. (2016b) show that increasing vertical resolution resulted in a greater deviation compared with the VOF/RANS simulation. The predicted v_t/v below the

trough levels by the original model, on the other hand, are considerably larger (up to 300%) than that reported in Lin and Liu (1998), especially in the outer surf zone and the transition region. We believe that the overprediction of v_t in the original model causes an unphysical uniform undertow current shown in Fig. 8C, D, and that the use of an unphysical dynamic boundary conditions at the surface leads to the distortion of wave shape from the expected sawtooth shape in the surf zone as shown in Figs. 6 and 7. As a result, the shock condition near the wave front becomes relatively weaker and thus the wave energy dissipation imposed by the numerical scheme is reduced. Due to an unphysical zero-vertical shear boundary condition at the free surface, $\partial u/\partial \sigma = 0$, and the resultant inaccurate near-surface velocity distribution above the trough levels the physical dissipation is also underpredicted, leading to the underprediction of the total wave-breaking-induced energy dissipation and the overprediction of wave heights in the surf zone as shown in Fig. 5.

Close to the bore-front regions, the values of v_t predicted by the new model are significantly smaller than those reported in Lin and Liu (1998) (Fig. 9a–e) due to a zero-tangential-stress boundary condition imposed at the smooth free surface. In the present study, as well as in all comparable derivations of non-hydrostatic

models, a zero-tangential-stress boundary condition is imposed at the smooth free surface, when wind is absent. However, in the case of the existence of high turbulence near the free surface such as in the bore-front region tangential stress at the smooth free-surface location ($\sigma = 1$) includes the Reynolds-type stress associated with roughness and intermittency in a finite region around the mean surface. The use of a smooth surface in such instances implies the pre-application of a subgrid smoothing filter to both the surface position and local velocity field. This smoothing has not been applied consistently in any of the presently available models of this type (see, for more details, Brocchini and Peregrine, 2001, Section 5). Inclusion of the turbulence-induced stress at the free surface should further improve model predictions of wave-breaking-induced near-surface velocity and turbulence fields. We will examine such parameterization in the near future.

6. Conclusions

In this paper, we derived the consistent surface and bottom dynamic boundary conditions for the velocity and dynamic pressure fields, using the appropriate dynamic boundary conditions on normal and tangential stresses at the top and bottom interfaces. A Neumann-type boundary condition for scalar fluxes was also derived. We focused on the examination of the role of surface slopes in the predicted near-surface velocity and turbulence fields in surface gravity waves, and thus the density field was assumed to be constant in all considered cases.

By comparing the predicted velocity field in a deep-water standing wave in a closed basin, we showed that the consistent boundary conditions did not generate unphysical vorticity at the free surface, in contrast to commonly used, simplified stress boundary conditions developed by ignoring all contributions except vertical shear in the transformation of stress terms.

In addition, we found that the consistent boundary conditions significantly improve the predicted velocity and turbulence fields in regular surf zone breaking waves, compared with the original model. The predicted wave shapes and wave height evolution were also improved by the new model. It was shown that the RNG-based $k - \epsilon$ model gave a better estimation of k compared with the standard $k - \epsilon$ model, especially in the transition region. Using the former also gave a better estimation of the wave phase-speed compared with that predicted by the latter. Predicted wave height and wave set-up variations by the various $k - \epsilon$ models, however, were approximately similar.

Acknowledgments

This work was supported by ONR, Littoral Geosciences and Optics Program (grant N00014-13-1-0124), NSF, Physical Oceanography Program (grant OCE-1435147) and Engineering for Natural Hazards (grants CMMI-1537100 and CMMI-1537232), and through the use of computational resources provided by Information Technologies at the University of Delaware. We thank the reviewers, whose thoughtful input led to significant improvements in the final manuscript.

References

- Banner, M.L., Peregrine, D.H., 1993. Wave breaking in deep water. *Ann. Rev. Fluid Mech.* 25, 373–397.
- Bradford, S.F., 2000. Numerical simulation of surf zone dynamics. *J. Waterway Port Coast. Ocean Eng.* 126, 1–13.
- Bradford, S.F., 2011. Nonhydrostatic model for surf zone simulation. *J. Waterway Port Coast. Ocean Eng.* 137, 163–174.
- Bradford, S.F., 2012. Improving the efficiency and accuracy of a nonhydrostatic surf zone model. *Coastal Eng.* 65, 1–10.
- Bradford, S.F., 2014. A mode split, godunov-type model for nonhydrostatic, free surface flow. *Int. J. Num. Meth. Fluids* 75, 426–445.
- Brocchini, M., Peregrine, D., 2001. The dynamics of strong turbulence at free surfaces. Part 2. free-surface boundary conditions. *J. Fluid Mech.* 449, 255–290.
- Derakhti, M., Kirby, J.T., Shi, F., Ma, G., 2014. Bubble entrainment and liquid-bubble interaction under unsteady breaking waves. *J. Fluid Mech.* 761, 464–506.
- Derakhti, M., Kirby, J.T., 2016. Breaking-onset, energy and momentum flux in focused wave packets. *J. Fluid Mech.* 790, 553–581.
- Derakhti, M., Kirby, J.T., Shi, F., Ma, G., 2015. NHWAVE: Model revisions and tests of wave breaking in shallow and deep water. Res. Rep. CACR-15-18, Center for Applied Coastal Research, Dept. of Civil and Env. Engineering, University of Delaware.
- Derakhti, M., Kirby, J.T., Shi, F., Ma, G., 2016a. Wave breaking from surf zone to deep water in a non-hydrostatic RANS model. Part 1: organized wave motions. *Ocean Mod.* in press.
- Derakhti, M., Kirby, J.T., Shi, F., Ma, G., 2016b. Wave breaking from surf zone to deep water in a non-hydrostatic RANS model. Part 2: turbulence and mean circulation. *Ocean Mod.* in press.
- Duncan, J.H., 2001. Spilling breakers. *Ann. Rev. Fluid Mech.* 33, 519–547.
- Kim, D., Lynett, P.J., Socolofsky, S.A., 2009. A depth-integrated model for weakly dispersive, turbulent, and rotational fluid flows. *Ocean Mod.* 27, 198–214.
- Lin, P., Li, C.W., 2002. A σ -coordinate three-dimensional numerical model for surface wave propagation. *Int. J. Num. Methods Fluids* 38, 1045–1068.
- Lin, P., Liu, P.-F., 1998. A numerical study of breaking waves in the surf zone. *J. Fluid Mech.* 359, 239–264.
- Ma, G., Chou, Y., Shi, F., 2014. A wave-resolving model for nearshore suspended sediment transport. *Ocean Mod.* 77, 33–49.
- Ma, G., Kirby, J.T., Shi, F., 2013. Numerical simulation of tsunami waves generated by deformable submarine landslides. *Ocean Mod.* 69, 146–165.
- Ma, G., Shi, F., Kirby, J.T., 2011. A polydisperse two-fluid model for surf zone bubble simulation. *J. Geophys. Res.* 116, C05010.
- Ma, G., Shi, F., Kirby, J.T., 2012. Shock-capturing non-hydrostatic model for fully dispersive surface wave processes. *Ocean Mod.* 43, 22–35.
- Melville, W.K., 1996. The role of surface-wave breaking in air-sea interaction. *Ann. Rev. Fluid Mech.* 28, 279–321.
- Perlin, M., Choi, W., Tian, Z., 2013. Breaking waves in deep and intermediate waters. *Ann. Rev. Fluid Mech.* 45, 115–145.
- Rodi, W., 1980. Turbulent models and their application in hydraulics—a state of the art review. *Int. Assoc. for Hydraul. Res., Delft.*
- Shi, F., Kirby, J.T., Harris, J.C., Geiman, J.D., Grilli, S.T., 2012. A high-order adaptive time-stepping TVD solver for boussinesq modeling of breaking waves and coastal inundation. *Ocean Mod.* 43, 36–51.
- Smit, P., Zijlema, M., Stelling, G., 2013. Depth-induced wave breaking in a non-hydrostatic, near-shore wave model. *Coastal Eng.* 76, 1–16.
- Stansby, P.K., Zhou, J.G., 1998. Shallow-water flow solver with non-hydrostatic pressure: 2d vertical plane problems. *Int. J. Num. Methods Fluids* 28, 541–563.
- Svendsen, I.A., 1987. Analysis of surf zone turbulence. *J. Geophys. Res.* 92 (C5), 5115–5124.
- Ting, F.C.K., Kirby, J.T., 1994. Observation of undertow and turbulence in a laboratory surf zone. *Coastal Eng.* 24, 51–80.
- Watanabe, Y., Saeki, H., Hosking, R.J., 2005. Three-dimensional vortex structures under breaking waves. *J. Fluid Mech.* 545, 291–328.
- Wei, G., Kirby, J.T., Grilli, S.T., Subramanya, R., 1995. A fully nonlinear boussinesq model for surface waves. Part 1. highly nonlinear unsteady waves. *J. Fluid Mech.* 294, 71–92.
- Wiegel, R., 1960. A presentation of cnoidal wave theory for practical application. *J. Fluid Mech.* 7, 273–286.
- Yakhot, V., Orszag, S., Thangam, S., Gatski, T., Speziale, C., 1992. Development of turbulence models for shear flows by a double expansion technique. *Phys. Fluids* 4, 1510–1520.